



Research paper

AgBr-wrapped Ag chelated on nitrogen-doped reduced graphene oxide for water purification under visible lightLili Zhang^a, Yilun Shi^c, Liang Wang^{c,d}, Chun Hu^{a,b,e,*}^a Key Laboratory of Drinking Water Science and Technology, Research Center for Eco-Environmental Sciences, Chinese Academy of Sciences, Beijing 100085, China^b School of Environmental Sciences and Engineering, Guangzhou University, Guangzhou 510006, China^b School of Environmental Sciences and Engineering, Guangzhou University, Guangzhou 510006, China^c School of Environmental and Chemical Engineering, Tianjin Polytechnic University, Tianjin 300387, China^d State Key Laboratory of Separation Membranes and Membrane Processes, Tianjin Polytechnic University, Tianjin 300387, China^e University of Chinese Academy of Sciences, Beijing 100049, China

ARTICLE INFO

Keywords:

AgBr@Ag/N-RGO

Interfacial contact

Visible light

Photocatalytic

Pollutants degradation

ABSTRACT

A visible-light-driven photocatalyst AgBr@Ag/nitrogen-doped reduced graphene oxide (AgBr@Ag/N-RGO) was prepared by a hydrothermal-*in situ* oxidation method, and characterized by scanning and transmission electron microscope, X-ray diffraction, Fourier-transform infrared spectra, Raman and X-ray photoelectron spectroscopy. AgBr@Ag/N-RGO exhibited high photoactivity and photostability to degrade and mineralize various organic pollutants, as demonstrated with 2-chlorophenol, phenol, bisphenol A and diphenhydramine in water under visible light. Its photoactivity was 20, 5.3, and 2.9 times higher than that of Ag/N-RGO, TiO_{2-x}N_x, and AgBr@Ag, respectively for the photodegradation of 2-chlorophenol. The characterized results verified that Ag nanoparticles (NPs) was first chelated by N-groups of N-RGO and then enwrapped by AgBr by *in-situ* oxidation, which was contributed to the enhancement of interfacial electron transfer in AgBr@Ag/N-RGO. Furthermore, the two charge transfer processes were elucidated that the plasmon-induced electrons on Ag NPs core transferred to AgBr shell, and could be further transferred away together with the photoexcited electrons on AgBr by N-RGO to interact with O₂ to form O₂^{·-}, while the electrons of pollutants were accelerated to transfer to the plasmon-induced Ag NPs by the Ag-N complex along the π-π graphitic carbon network of N-RGO, which was responsible for the photoactivity and stability of AgBr@Ag/N-RGO.

1. Introduction

Natural organic compounds and synthetic organic micro-contaminants such as phenols, pharmaceuticals and pesticides, are constantly being released into the environment [1]. Due to their toxicity, such pollutants have strict discharge limits. Heterogeneous photocatalysis has been considered as a promising and green chemical process for the removal of organic contaminants in water [2]. To optimize the use of solar energy and reduce costs and energy consumption for photocatalytic water purification, we require efficient and stable photocatalysts that are capable of harvesting visible light [3].

As a potential alternative, introducing plasmonic Au or Ag nanoparticles (NPs) onto semiconductor materials have been shown to effectively enhance the photocatalytic activity in the visible region due to the strong surface plasmon resonance (SPR) [4–7]. For example, plasmonic Ag NPs on Ag₃PO₄ and AgCl can promote the photocatalytic

efficiency and enhance the stability of these Ag-based photocatalysts [8,9]. Silver bromide (AgBr) has been used as an attractive small bandgap semiconductor because of its unique light-sensitive and ionic transport properties [10]. In general, pure AgBr is unstable under light irradiation. According to recent reports, AgBr might serve as stable and active cocatalyst under visible irradiation by coupling with Ag [11], which mainly depends on the photogenerated charge transfer between the formed nanoheterostructured composites. Actually, the structural and electronic properties of semiconductor materials can also be facilely improved by the appropriate cocatalysts or supports.

Graphene including graphene oxide (GO) and reduced graphene oxide (RGO), a unique sp² hybrid carbon network material, has been used as an ideal cocatalyst or support to improve the photocatalytic efficiency owing to high electron mobility, high surface area, and high transparency, [12]. Doping the carbon network of graphene with heteroatoms (e.g., N, B, and P) could increase the catalytic active sites,

* Corresponding author at: Key Laboratory of Drinking Water Science and Technology, Research Center for Eco-Environmental Sciences, Chinese Academy of Sciences, Beijing, 100085, China.

E-mail address: huchun@rcees.ac.cn (C. Hu).

electrical conductivity and surface hydrophilicity [13]. Moreover, previous research has shown N-groups on reduced GO can serve as favourable nucleation and anchor sites for metal NPs or metal oxides [14,15]. This paper intends to anchor AgBr-coated Ag on N-doped RGO and investigate the photocatalytic performance of AgBr@Ag/N-RGO for wastewater treatment under visible light.

In the present study, we report AgBr-wrapped Ag nanoparticles chelated on N-doped RGO by N groups prepared with a facile hydrothermal-*in situ* oxidation method. The properties of the AgBr@Ag/N-RGO photocatalyst such as morphology, crystal structure, optical property, electrochemical characteristics, and photocatalytic activity were systematically characterized and evaluated by multi-technologies. The mechanism of the enhanced photocatalytic activity and photo-stability was proposed.

2. Experimental

2.1. Materials

Silver nitrate (AgNO_3), potassium bromide (KBr) and graphite powder were purchased from Sinopharm Chemical Reagent Co., Ltd. 5-tert-Butoxycarbonyl-5-methyl-1-pyrrolidine-N-oxide (BMPO) was supplied by the Bioanalytical Lab (Sarasota, FL). 2-Chlorophenol (2-CP), phenol, bisphenol A (BPA) and diphenhydramine (DP) were obtained from Aros (Geel, Belgium). All chemicals were at least analytical grade.

2.2. Preparation of catalysts

The GO was obtained by chemical exfoliation of natural graphite following the modified Hummers' method [16]. The GO aqueous solution was prepared by ultrasonic dispersion of GO powder in water for 2 h. For the synthesis of Ag/N-RGO, the GO aqueous solution (0.05 wt %) was mixed with silver ammonia solution (0.1 M AgNO_3 in 3 M $\text{NH}_3\text{H}_2\text{O}$) and hydrothermally treated at 130 °C for 3 h. After cooling down to room temperature, the resulting samples were centrifuged, washed and dried in vacuum at 60 °C for 5 h. Following this procedure, Ag/N-RGO (x wt%) were obtained, where x referred to the weight ratios of GO to Ag in the preparation process. 0.5 g of the as-prepared Ag/N-RGO (x wt%) was added into a freshly prepared FeBr_3 aqueous solution (0.1 M) and stirred for 30 min. After centrifuging, repeated rinsing with deionized water and drying in vacuum at 60 °C for 5 h, AgBr@Ag/N-RGO (x wt%, y) was obtained, where y represented the volume of FeBr_3 added in the preparation process. The AgBr@Ag/N-RGO (3 wt%, 40) photocatalyst exhibited the highest photocatalytic activity and stability, as shown in Fig. S1 and Table S1. This catalyst was used for all of the subsequent experiments unless otherwise specified. For comparison, AgBr@Ag was obtained by calcinating Ag/N-RGO (3 wt%) at 500 °C to remove N-RGO and then *in situ* oxidation by 40 mL of 0.1 M FeBr_3 for 30 min at room temperature. N-RGO was prepared by hydrothermally treating the mixture of GO aqueous solution (0.05 wt%) and ammonia solution (3 M) at 130 °C for 3 h. In addition, RGO, Ag/RGO and AgBr@Ag/RGO were synthesized through the same steps used for making N-RGO, Ag/N-RGO and AgBr@Ag/N-RGO without adding $\text{NH}_3\text{H}_2\text{O}$, respectively. As the standard example of a visible-light photocatalyst, $\text{TiO}_{2-x}\text{N}_x$ was prepared via a previously reported method [17].

2.3. Characterization

Morphological studies were carried out using a field emission scanning electron microscope (FESEM, Hitachi, SU8020). The high resolution transmission electron microscopy (HRTEM) images of the samples were obtained using a JEOL-2010 TEM with an acceleration voltage of 200 kV. Powder X-ray diffraction (XRD) patterns were recorded using a Scintag-XDS-2000 diffractometer with Cu K α radiation ($\lambda = 1.540598 \text{ \AA}$). The generator voltage and tube current used were

40 kV and 40 mA, respectively. Fourier-transform infrared (FTIR) spectra were obtained using a Bruker Tensor 27 FTIR Spectrophotometer. For FTIR, powdered specimens were diluted with KBr at a ratio of 1:100, and pressed into a pellet. X-ray photoelectron spectroscopy (XPS) data were measured via an AXIS-Ultra instrument from Kratos using monochromatic Al K α radiation (225 W, 15 mA, 15 kV) and low-energy electron flooding for charge compensation. To compensate for surface charge effects, binding energies were calibrated using the C1s hydrocarbon peak at 284.8 eV. Raman spectra were recorded on a LabRAM HR Evolution (HORIBA, France) equipped with a CCD detector using a laser source at an excitation line of 532 nm. UV-vis diffuse reflectance spectra were collected on a Shimadzu U3900 recording spectrophotometer equipped with an integrating sphere. ESR spectra were obtained using a Bruker model ESP 300E electron paramagnetic resonance spectrometer. Photoelectrochemical measurements were mainly performed using a conventional three-electrode cell system and a CHI 660D electrochemical workstation. The photocatalyst electrode was employed as the working electrode, and a platinum electrode and a saturated calomel electrode served as the counter and reference electrodes, respectively. To prepare the photocatalyst electrode, 50 mg of photocatalyst powders was dispersed ultrasonically in 1 mL of 0.5 wt% Nafion solution, and 0.1 mL of the resulting colloidal dispersion was drop-cast onto the indium-tin oxide (ITO) conducting glass with a fixed area of 1.0 cm^2 and dried under ambient conditions. The electrochemical impedance spectroscopy (EIS) was operated in the frequency range of 0.1–10⁵ Hz in 0.1 M Na_2SO_4 solution.

2.4. Procedures and analysis

The photocatalytic activities of the samples were evaluated by the degradation of various organic pollutants under 150 W Xe arc lamp with a 400 nm cutoff filter at room temperature and neutral pH. The incident visible light intensity was 3.5 mW cm^{-2} , which was measured with a radiometer (Photoelectric Instrument Factory Beijing Normal University). Unless indicated otherwise, 1.6 g L^{-1} catalysts were dispersed in 0.078 mM organic pollutants solution with constant stirring. Prior to irradiation, the suspensions were stirred in the dark for 30 min to ensure adsorption-desorption equilibrium. At given time intervals, part of the suspension sample was withdrawn and filtered to remove powders for analysis. The concentration of organic pollutants was measured using high-performance liquid chromatography (1200 series; Agilent) with a Zorbax SB-Aq column (5 μm , 4.6 × 250 mm; Agilent). The total organic carbon (TOC) of the solution was analyzed using a TOC-V_{CPH} analyzer (Shimadzu). The measurements of bromide ion (Br^-), chloride ion (Cl^-) and short-chain organic acids were conducted using a Dionex model ICS 2000 ion chromatograph (IC) equipped with an IonPac AS11-HC analytical column (4 × 250 mm) and using 40 mM KOH as an eluent.

In addition, the possible Ag^+ leaching during the reaction was monitored by inductively coupled plasma optical emission spectroscopy (ICP-OES) on an Optima 2000 (PerkinElmer, Inc.) instrument. To test the stability and recyclability of AgBr@Ag/N-RGO, the catalyst was filtered, washed with water, and dried at 60 °C. The catalyst was continued to be used in the second cycle. This process was repeated several times.

All of the above experiments were repeated in triplicate and data represented the average of the triplicates with a standard deviation of less than 5%.

3. Results and discussion

3.1. Characterization of catalysts

N-RGO showed a transparent, thin and wrinkled morphology (Fig. S2A), which displayed the typical graphene structure. The elemental mappings of N-RGO (Fig. S2B) confirmed the existence of N in the

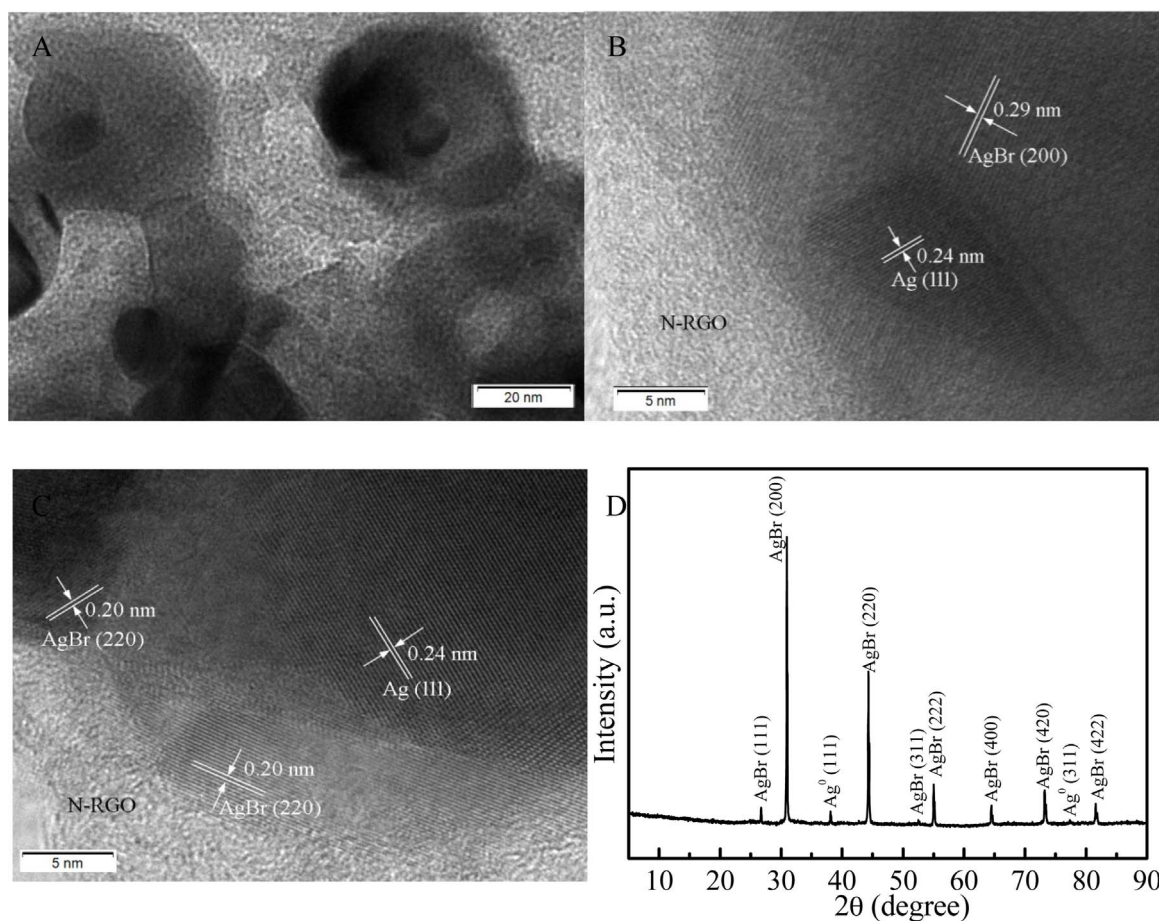


Fig. 1. TEM image (A), HRTEM images (B and C), and XRD pattern (D) of AgBr@Ag/N-RGO.

matrix. Compared to RGO, the XPS scan spectra of N-RGO exhibited the existence of the N 1s peak (Fig. S2C). The high-resolution N 1s spectra mainly showed two peaks with binding energies of 398.5 eV and 399.7 eV, corresponding to pyridinic and pyrrolic nitrogen species in N-RGO, respectively.

The morphologies of Ag/N-RGO and AgBr@Ag/N-RGO were observed by FESEM and TEM, as shown in Figs. S2 and 1. For Ag/N-RGO, Ag NPs with a diameter from 20 nm to 97 nm were formed on the N-RGO sheets (Fig. S3A, C and D). After the oxidation reaction of Ag/N-RGO in freshly prepared FeBr₃ aqueous solution, the morphology was transformed to irregular dried-mud-like structure (Fig. S3B). The TEM image of AgBr@Ag/N-RGO (Fig. 1A) showed that core-shell-like nanoparticles was observed on the surface of the plate-like substrate. A deeper inspection of the microstructure of AgBr@Ag/N-RGO using HRTEM (Fig. 1B and C) showed the presence of lattice fringes at 0.24 nm attributed to the (111) d-spacing of Ag. And the lattice fringes of 0.29 nm and 0.20 nm were observed on the outer surface of Ag, which corresponded to the (200) and (220) planes of AgBr, respectively, indicating that Ag was entirely or partly wrapped by AgBr. In addition, an amorphous zone correlated to N-RGO was visible in Fig. 1B and C. These results preliminarily suggested the formation of AgBr-wrapped Ag on N-RGO.

The XRD patterns of the different samples were shown in Figs. S4 and 1D. A (002) diffraction peak at 12.1° was observed for GO, suggesting most of the natural graphite was oxidized into GO by expanding the d-spacing from 0.34 nm to 0.73 nm, and oxygen functional groups were introduced on the GO sheets [18]. After the hydrothermal treatment with the addition of ammonia, the sharp diffraction peak of GO disappeared while a weak and broad diffraction peak at 23.8° appeared. The largely reduced (002) interlayer spacing of 0.37 nm in comparison

with 0.73 nm of GO revealed that most of the oxygen functional groups intercalated into the interlayer spacing of graphite had been removed during this reduction process. The diffraction peaks of Ag/N-RGO were well assigned to metallic Ag (JCPDS 65-2871). After the oxidation reaction of Ag/N-RGO in freshly prepared FeBr₃ aqueous solution, the characteristic peaks corresponding to AgBr phase (JCPDS 79-0149) could be clearly observed and the corresponding diffraction peaks of metallic Ag significantly decreased. Notably, negligible diffraction peaks ascribed to N-RGO could be detected by XRD, which might be due to the relatively low content and low diffraction intensity of N-RGO in Ag/N-RGO and AgBr@Ag/N-RGO [19]. In addition, the characteristic peaks of Ag and AgBr appeared in the XRD pattern of AgBr@Ag.

The reduction of GO was further confirmed by the FTIR spectra. In the spectrum of GO (Fig. S5), the absorption peaks at 1728, 1225 and 1053 cm⁻¹ can be ascribed to stretching vibrations of C=O, C—OH and C—O, respectively [16]. The broad and intense peak centered at 3371 cm⁻¹ corresponded to the absorption of hydroxyl groups on GO surface and adsorbed water molecules. And the peak at 1620 cm⁻¹ was assigned to the vibrations of the adsorbed water molecules and also the contributions from the skeletal vibrations of unoxidized graphitic domains. After the hydrothermal treatment with the addition of ammonia solution, the oxygen-containing functional groups at 1728 and 1225 cm⁻¹ disappeared, and the intensity of the peaks around 3371, 1620 and 1053 cm⁻¹ was greatly suppressed as shown in Fig. 2, indicating the GO has been reduced for Ag/N-RGO and AgBr@Ag/N-RGO [20]. Meanwhile, the peaks at 3371 and 1620 cm⁻¹ shifted to 3435 and 1631 cm⁻¹, respectively, indicating the existence of N—H and the formation of Ag-N complex in Ag/N-RGO [21]. The two peaks further shifted to 3456 and 1615 cm⁻¹ for AgBr@Ag/N-RGO, probably due to the complexation of Ag⁺ in AgBr to N groups of N-RGO [22]. In

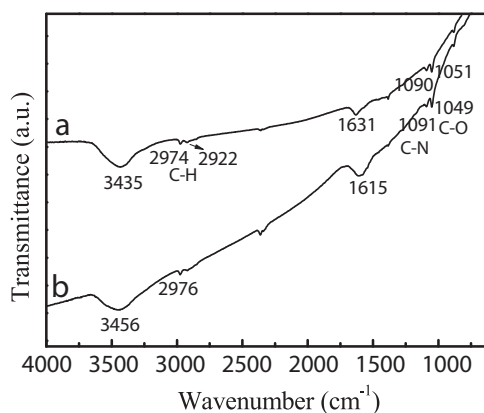


Fig. 2. FTIR of (a) Ag/N-RGO and (b) AgBr@Ag/N-RGO.

addition, a new band around 1090 cm^{-1} corresponding to C–N stretching vibration appeared in Ag/N-RGO and AgBr@Ag/N-RGO. And a triplet at about 2922 cm^{-1} attributed to C–H bonds was also visible in the FT-IR spectra of Ag/N-RGO and AgBr@Ag/N-RGO, which was correlated to the presence of O and N bearing functionalities [23].

Fig. 3 showed the Raman spectra of GO, N-RGO, Ag/N-RGO and AgBr@Ag/N-RGO. Two characteristic peaks of the graphitic material, namely D and G bands, were observed at around 1348 cm^{-1} and 1600 cm^{-1} . The G band was a characteristic of sp^2 hybridized carbon materials, which could provide information on the inplane vibration of sp^2 -bonded carbon domains. On the other hand, the D band corresponded to the disorder band indicating the presence of sp^3 defects within the graphitic structure and associated with the amorphous carbon, or edges that broke the symmetry and selection rule [24]. The ratio of the D band and G band intensities ($I_{\text{D}}/I_{\text{G}}$) of N-RGO (1.09) was significantly higher than that of GO (0.81), indicating the production of the sp^2 domains in N-RGO after the reduction of oxygen-containing groups in GO [25]. The further increased $I_{\text{D}}/I_{\text{G}}$ of Ag/N-RGO (1.21) compared to that of N-RGO (1.09) indicated the formation of more defects in carbon, probably due to the strongly coupled interaction between Ag NPs and N-RGO by N groups, in line with the formation of Ag–N complex confirmed by FT-IR. The $I_{\text{D}}/I_{\text{G}}$ of AgBr@Ag/N-RGO (1.02) was lower than that of Ag/N-RGO (1.21) and nearly equal to that of N-RGO (1.09) indicated the partial restoration of the defects through the oxidation of Ag by Fe^{3+} ions [12].

To further verify the structure of AgBr@Ag/N-RGO, the surface elemental compositions were characterized by XPS. The XPS scan spectra of AgBr@Ag/N-RGO exhibited distinct Ag 3d, Br 3d, C 1s, N 1s and O 1s peaks (Fig. S6A), revealing the predominant presence of Ag, Br, C, N and O elements. The high-resolution C 1s spectrum (Fig. S6B) showed the existence of C–C/C=C at 284.6 eV , C=N and C–OH at 285.6 eV , C–O–C at 286.5 eV , C–N and C=O at 287.4 eV and O=C–O at

288.9 eV [26]. Compared with those of GO-involved photocatalysts [27], the intensities for peaks corresponding to the epoxy/ether group, the carbonyl carbon and the carboxylate carbon exhibited smaller relative contents, indicating the successful removal of oxygen-containing groups and intact restoration of the extensive conjugated sp^2 carbon network. Specially, XPS revealed 2.61 at% nitrogen in AgBr@Ag/N-RGO, indicating the successful doping of nitrogen in RGO. The high-resolution N 1s spectra (Fig. S6C) showed two peaks with binding energies of 398.9 eV and 400.2 eV , corresponding to pyridinic and pyrrolic nitrogen species in AgBr@Ag/N-RGO. N-groups on RGO could serve as favourable nucleation and anchor sites for Ag NPs owing to coordination with Ag cations [15], thus a strong coupling between Ag and N-RGO probably existed in AgBr@Ag/N-RGO, in agreement with the results of FT-IR and Raman. The Ag 3d_{5/2} and Ag 3d_{3/2} peaks for AgBr@Ag/N-RGO appeared at binding energies of 367.4 eV and 373.4 eV , which was significantly lower than the values measured for Ag/N-RGO (Fig. 4A), suggesting the surface Ag species mainly existed as Ag^+ in AgBr@Ag/N-RGO [28]. Furthermore, auger electron spectroscopy (AES) measurements were performed. The auger parameter at 724.1 eV was assigned to Ag^+ , lower than that of Ag^0 in Ag/N-RGO (Fig. 4B), further indicating that the surface Ag species of AgBr@Ag/N-RGO were mainly Ag^+ [29]. The peaks of Br 3d_{5/2} and Br 3d_{3/2} at 68.0 eV and 69.0 eV (Fig. S6D), respectively, were attributed to the Br^- in AgBr. Moreover, the concentration of the surface Ag and Br was 17.88 at% and 14.35 at%, respectively. The atomic ratio of Ag and Br was about 1.25 approximately equal to the stoichiometric ratio of AgBr, indicating the Ag^0 was mainly coated by AgBr, in line with the results of TEM.

Fig. 5 showed the typical UV-vis diffuse reflectance spectra of GO, RGO, N-RGO, Ag/N-RGO and AgBr@Ag/N-RGO. It could be seen that GO displayed a broad absorption band maximum around 270 nm and 390 nm , which was accompanied by a tail absorption between 400 and 800 nm . Compared to the absorbance spectra for GO aqueous solution with absorption band maximum at 230 nm and 300 nm assigned to $\pi-\pi^*$ and $n-\pi^*$ transitions [25] (Fig. S7), the spectral broadening and change in the absorption position were attributed to the dense packing of GO powders and to the different dielectric constants of water and air [30]. Compared with GO, RGO and N-RGO showed a markedly increased tail absorption between 400 and 800 nm . The absorbance spectra of RGO and N-RGO aqueous solution (Fig. S8) showed that the $\pi-\pi^*$ transition band shifted from 230 nm to 255 nm and 272 nm , respectively, indicating the electronic conjugation was restored after the removal of oxygen groups. For the UV-vis diffuse reflectance spectra of Ag/N-RGO, a strong absorption band appeared at 320 nm , which should be due to the electrons directly bonded to the silver atoms that acted as bulk silver [31]. Compared with Ag/N-RGO, AgBr@Ag/N-RGO exhibited a broad absorption peak at about 550 nm , due to the surface plasmon resonance (SPR) of the residual Ag NPs after the oxidation of FeBr₃ [32].

3.2. Photocatalytic performance

The photocatalytic performances of various photocatalysts were tested under visible light irradiation ($\lambda > 400\text{ nm}$, 3.5 mW cm^{-2}). As shown in Fig. 6, less than 13% of 2-CP was photodegraded by Ag/N-RGO after reaction for 120 min. And the photodegradation of 2-CP within 40 min was only 17% and 35% in the AgBr@Ag/RGO and AgBr@Ag suspensions, respectively. Under identical experimental conditions, 19% of 2-CP was photodegraded by TiO_{2-x}N_x, which is considered the standard example of the visible-light photocatalyst [33]. After *in situ* oxidizing Ag/N-RGO into AgBr@Ag/N-RGO, the photodegradation rate of 2-CP significantly increased and nearly complete removal of 2-CP was reached within 40 min, which was 20, 5.3, and 2.9 times faster than that in Ag/N-RGO, TiO_{2-x}N_x, and AgBr@Ag suspensions, respectively. And the TOC removal rate of 2-CP was more than 79% within 120 min in AgBr@Ag/N-RGO suspension. During the photodegradation

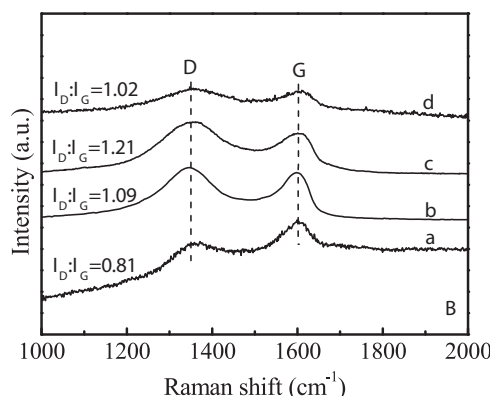


Fig. 3. Raman spectra of (a) GO, (b) N-RGO, (c) Ag/N-RGO, and (d) AgBr@Ag/N-RGO.

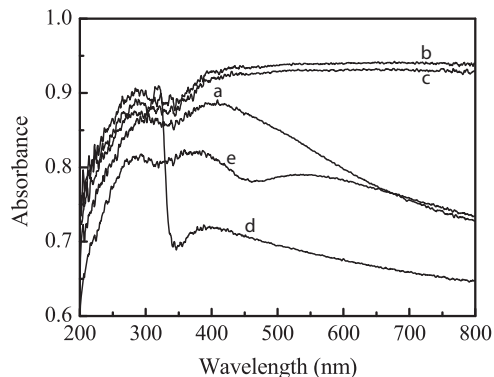
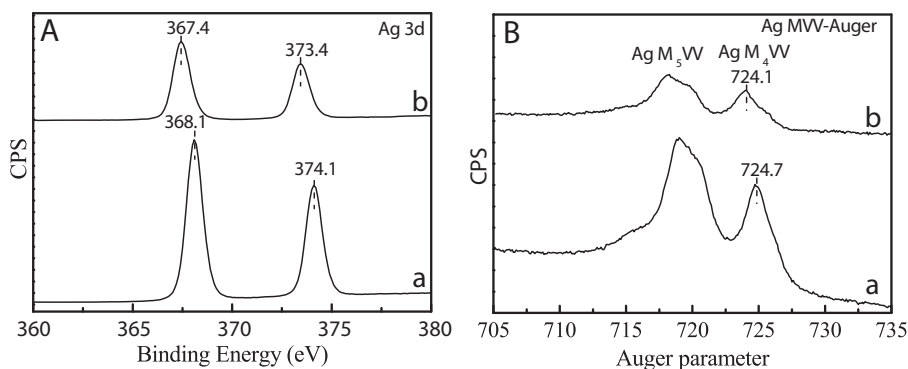


Fig. 5. UV-vis diffuse reflectance spectra of (a) GO, (b) RGO, (c) N-RGO, (d) Ag/N-RGO, and (e) AgBr@Ag/N-RGO.

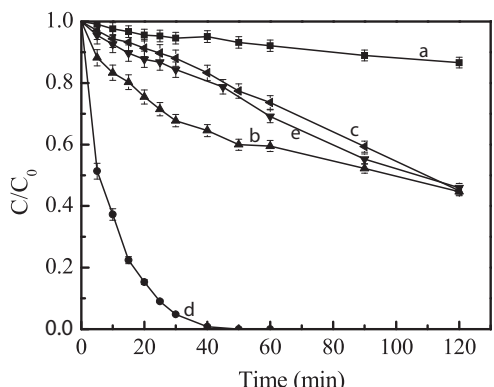


Fig. 6. Photodegradation of 2-CP (0.078 mM) under visible light ($\lambda > 400$ nm) in different suspensions (1.6 g L⁻¹): (a) Ag/N-RGO, (b) AgBr@Ag, (c) AgBr@Ag/RGO, (d) AgBr@Ag/N-RGO, and (e) TiO_{2-x}N_x.

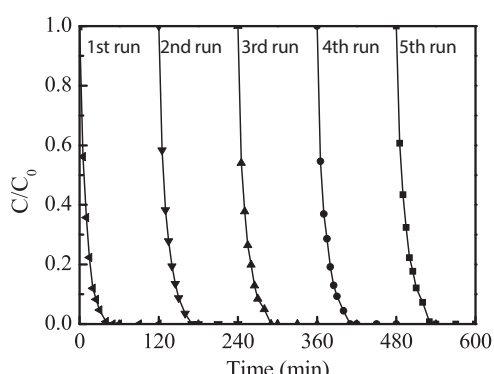


Fig. 7. Cycling runs in the photodegradation of 2-CP (0.078 mM) in AgBr@Ag/N-RGO aqueous dispersion (1.6 g L⁻¹) under visible light ($\lambda > 400$ nm).

of 2-CP, the concentration of dissolved metals was determined. After 120 min reaction, the amount of Ag(I) release was only 0.24 mg L⁻¹ in AgBr@Ag/N-RGO suspension. And the cycle tests exhibited that the conversion of 2-CP decreased by 7% in the fifth cycle of AgBr@Ag/N-RGO and remained at approximately 93% within 40 min in the continuous cycles (Fig. 7). Furthermore, no significant change was observed in the XRD pattern (Fig. S9, line a) and XPS spectra (Fig. S10) of AgBr@Ag/N-RGO after reaction. The results indicated that the catalyst had an excellent stability under visible light. In addition, the photo-oxidation experiments of AgBr@Ag/N-RGO carried out under full Xe arc light including UV and visible light, leading to the similar result. 2-CP could be completely degraded within 20 min in AgBr@Ag/N-RGO suspension under full Xe arc light. The photocatalytic activity did not markedly decrease after five successive cycles under full Xe arc light, and 2-CP could still be completely degraded within 30 min in the continuous cycles (Fig. S11). Furthermore, no significant change was observed in the XRD pattern (Fig. S9, line b) of AgBr@Ag/N-RGO after reaction under full Xe arc light. Thus, AgBr@Ag/N-RGO is a photocatalyst active and stable under UV and visible light.

The changes of some intermediates were followed by the degradation of 2-CP in Fig. S12. The generation of Cl⁻ was observed. The concentration of *p*-benzoquinone as one of the primary aromatic products increased and reached a maximum at 15 min, and then gradually decreased and completely disappeared within 90 min. Furthermore, maleic acid and malonic acid were detected in trace amounts. In summary, 2-CP was photooxidized into quinone products, subsequently into short-chain organic acids and eventually into CO₂ and H₂O.

In addition, AgBr@Ag/N-RGO also exhibited excellent photocatalytic activity in the degradation of phenol, BPA and DP under visible light. As shown in Fig. 8, the photodegradation rate of both phenol and BPA could be up to 88% within 120 min. And the corresponding TOC removal could reach 70% within 120 min, indicating the degradation and mineralization of both phenol and BPA was almost simultaneous. Moreover, refractory DP with N-containing side-chains could be degraded 70% with 4.8% of the TOC removal rate.

The high activity and stability of AgBr@Ag/N-RGO were probably related to the inhibited agglomeration of AgBr@Ag during its synthesis by N-RGO and the interfacial structures. The unique structure that AgBr-wrapped Ag dispersedly anchored on N-RGO would provide more active sites than AgBr@Ag. And the coupling between AgBr@Ag and N-RGO by N-groups could facilitate the interfacial charge transfer more efficiently.

3.3. Photoelectrochemical measurements

The transient photocurrent responses were recorded via several on-off cycles of irradiation to give evidence for the visible light activity of AgBr@Ag/N-RGO. As shown in Fig. 9A, a pronounced photocurrent density spike (J_{in}) can be observed for AgBr@Ag/N-RGO upon illumination with visible light, indicating the electron (e⁻)/hole (h⁺) pairs immediately generated and then separated in AgBr@Ag/N-RGO [34].

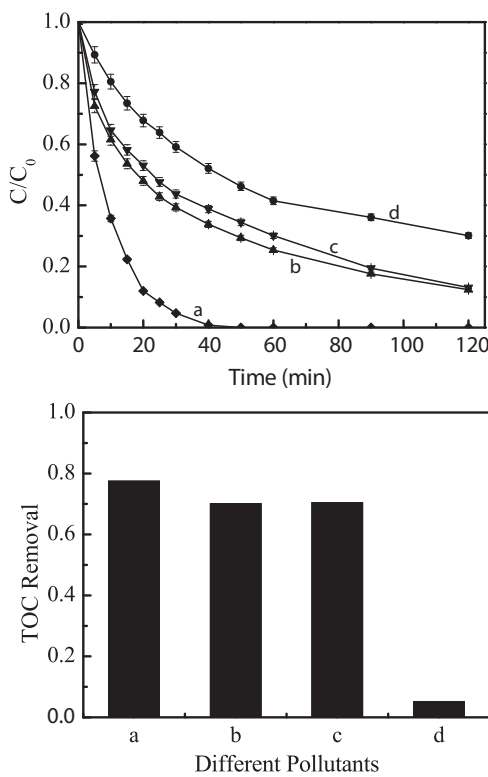


Fig. 8. Photodegradation of different pollutants (0.078 mM) in AgBr@Ag/N-RGO (1.6 g L^{-1}) suspensions under visible light ($\lambda > 400 \text{ nm}$): (a) 2-CP, (b) Phenol, (c) BPA, and (d) DP.

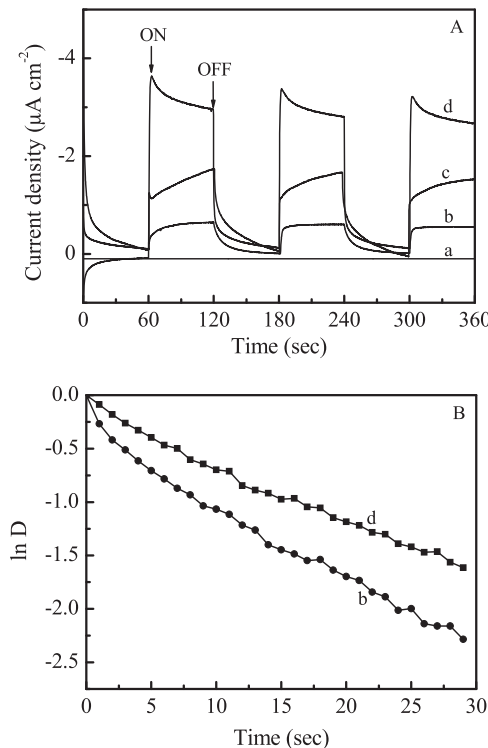


Fig. 9. Transient photocurrent response (A) and normalized plots of the photocurrent-time dependence (B) for (a) Ag/N-RGO, (b) AgBr@Ag, (c) AgBr@Ag/RGO and (d) AgBr@Ag/N-RGO under visible light ($\lambda > 400 \text{ nm}$).

Subsequently, J_{in} decreased in a decelerated fashion until equilibrium was reached, which could be attributed to the unavoidable e^-/h^+ recombination. Specially, the recombination probably occurred during

the transfer process, resulting in a decay of J_{in} . When the equilibrium was reached between the generation rate and recombination rate, a steady state photocurrent density (J_{st}) was achieved. After the illumination was switched off, the J_{st} rapidly dropped to almost zero, indicating the separated e^-/h^+ pairs immediately recombined due to the highly efficient charge transport. The transient photocurrent spikes in AgBr@Ag was not observed, suggesting that recombination in the bulk limited charge carrier transport [35]. And the steady state photocurrent density of AgBr@Ag/N-RGO, AgBr@Ag/RGO and AgBr@Ag was about $2.86 \mu\text{A cm}^{-2}$, $1.60 \mu\text{A cm}^{-2}$ and $0.74 \mu\text{A cm}^{-2}$, respectively, whereas that of Ag/N-RGO was almost zero. Furthermore, a normalized parameter (D) was derived from the transient photocurrent curve to quantitatively determine the charge recombination behavior, $D = (I_t - I_{st})/(I_{in} - I_{st})$, where I_t , I_{in} and I_{st} are the time-dependent, the initial and the steady-state photocurrents, respectively [36]. The normalized plots of $\ln D - T$ were shown in Fig. 9B. The transient time constant (τ), defined as the time when $\ln D = -1$ [36], was estimated to be 8.6 s and 16.4 s for AgBr@Ag and AgBr@Ag/N-RGO, respectively, confirming the suppression of charge recombination due to the existence of N-RGO to disperse AgBr@Ag and promote photogenerated charge carriers away from the AgBr@Ag surface.

The radius of the arc on the EIS Nyquist plot could reflect the reaction rate occurring at the surface of catalysts. The arc radius of AgBr@Ag/N-RGO was smaller than that of AgBr@Ag under visible light irradiation (Fig. 10), suggesting that the AgBr-wrapped Ag dispersely anchored on N-RGO would lead to a more effective separation of photogenerated e^-/h^+ pairs and faster interfacial charge transfer. All the above results proved that the good surface contact of AgBr, Ag and N-RGO could enhance the separation and transfer of photo-generated charge carriers, inhibiting the recombination of e^- and h^+ effectively and hence improving the photocatalysis efficiency.

3.4. Reaction mechanism

To identify the primary reactive species responsible for the photocatalytic oxidation of organic pollutants over AgBr@Ag/N-RGO under visible light irradiation, the effects of various radical scavengers on the degradation of 2-CP were examined in Fig. 11. The addition of the superoxide (O_2^-) scavenger *p*-benzoquinone strongly inhibited the degradation of 2-CP and only about 9% of 2-CP was degraded in AgBr@Ag/N-RGO suspension under visible light ($\lambda > 400 \text{ nm}$) within 40 min. And there was about 68% of 2-CP that was photodegraded with the addition of h^+ scavenger disodium ethylenediamine tetraacetate (EDTA-2Na). However, the degradation rate of 2-CP was hardly changed with the addition of hydroxyl radicals ($\cdot OH$) scavenger *t*-butanol. Furthermore, the BMPO spin-trapping ESR technique was used to detect the production of $\cdot OH$ and O_2^- (Fig. S13). No characteristic peaks of BMPO- $\cdot OH$ were observed in AgBr@Ag/N-RGO suspension under visible light irradiation, suggesting that $\cdot OH$ oxidation was not the main reaction during photocatalytic process. In fact, the valence

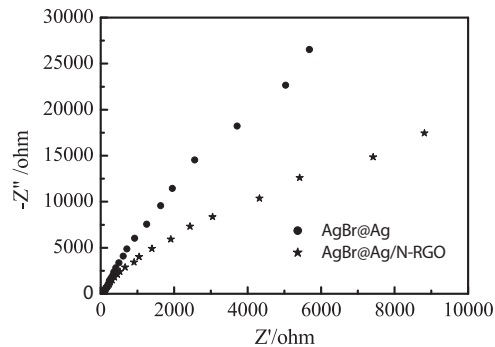


Fig. 10. EIS Nyquist plots of AgBr@Ag and AgBr@Ag/N-RGO under visible light irradiation.

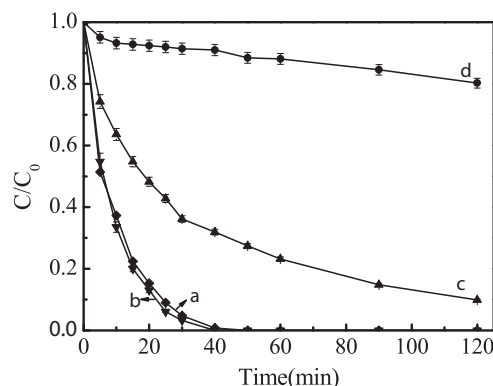


Fig. 11. Plotted degradation kinetics of 2-CP (0.078 mM) in $\text{AgBr}@\text{Ag}/\text{N-RGO}$ (1.6 g L^{-1}) suspensions under visible light ($\lambda > 400 \text{ nm}$) with (a) no scavenger added, (b) t-butanol (100 mM), (c) EDTA-2Na (1 mM), and (d) *p*-benzoquinone (1 mM).

band edge potential of AgBr was at about 2.16 eV [37], which was less positive than the standard reduction potential of $\cdot\text{OH}/\text{OH}^-$ (2.38 eV) [38,39], confirming that the h^+ on the surface of AgBr cannot oxidize OH^- into $\cdot\text{OH}$ kinetically. The characteristic peaks of $\text{BMPO-O}_2\cdot^-$ were obviously observed in $\text{AgBr}@\text{Ag}/\text{N-RGO}$ suspension under visible light irradiation, while little $\text{O}_2\cdot^-$ was detected in dark. The above results suggested that $\text{O}_2\cdot^-$ was the main reactive species in the photocatalytic process and h^+ was in part responsible for the pollutant degradation.

In principle, the different work functions of the AgBr (5.3 eV) and Ag (4.25 eV) would lead to the formation of Schottky barrier [40]. The close contact between AgBr and Ag would promote the electrons to transfer from Ag to AgBr until their Fermi levels were equilibrated. Due to the strong SPR effect of the interior Ag NPs, the electron would be enriched on the surface of the Ag^0 under visible light irradiation, which lifted the Fermi level of Ag . Subsequently, the energetic electrons from the plamon-excited Ag NPs migrated to the conduction band of AgBr . Simultaneously, electrons and holes were generated from the photo-excited AgBr shell under visible light irradiation. The electrons could be further transferred away from AgBr by N-RGO along the $\pi-\pi$ graphitic carbon network, where they can be trapped by O_2 to form $\text{O}_2\cdot^-$ (Scheme 1). In addition, Br^- was detected during 2-CP degradation in $\text{AgBr}@\text{Ag}/\text{N-RGO}$ suspension under visible light ($\lambda > 400 \text{ nm}$) (Fig. S14), and thus the photo-generated h^+ in the valence band of AgBr

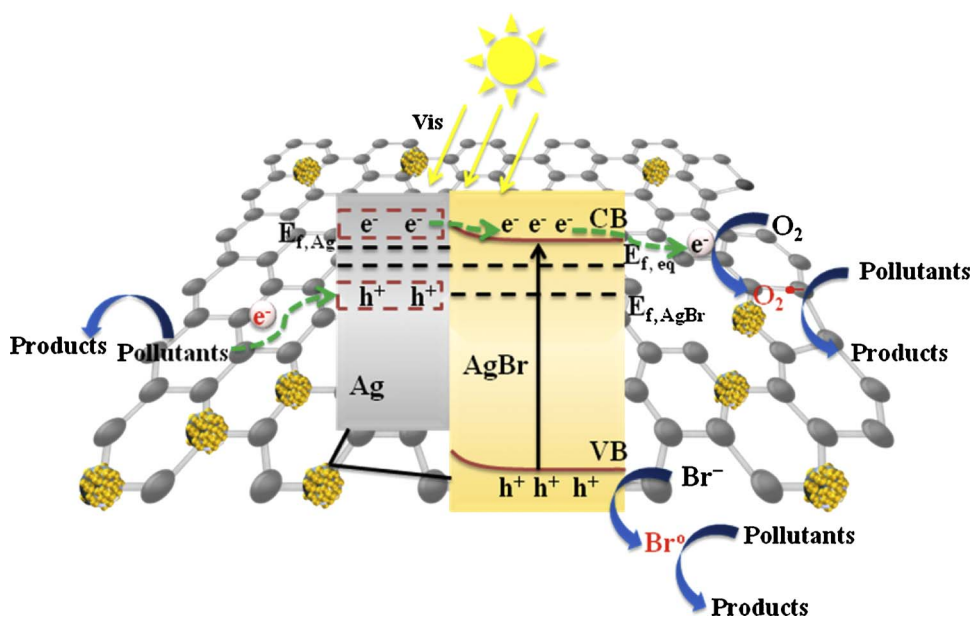
could combine with Br^- to form Br^0 [41], which were radicals with strong oxidation power and could also degrade and mineralize organic pollutants [42].

Meanwhile, the remaining holes in Ag NPs would be depleted by electrons transported through N-RGO from pollutants. The charge transfer processes were testified by cyclic voltammetry (CV) analysis. In an air-saturated 0.1 M Na_2SO_4 aqueous solution (Fig. S15), the oxidation peak of Ag NPs was observed under visible light irradiation [33]. And the peak decreased with the addition of DP to act as electron donors and became indiscernible when BPA, phenol and 2-CP at the same concentration with DP were added, respectively. The results revealed that these organic pollutants could be oxidized by plasmon-induced h^+ on Ag NPs, thus facilitating the photooxidized Ag NPs back to their initial state. This confirmed that plasmon-induced h^+ was one of the active species for the pollutants degradation and one electron transfer occurred from the organic pollutants to the Ag NPs. To understand the role of N-RGO during the electron transfer process, the $\text{AgBr}@\text{Ag}/\text{N-RGO}$ samples after pollutant sorption were characterized by FTIR (Fig. S16). The peak at 3456 cm^{-1} was shifted to around 3439 cm^{-1} after the selected pollutants sorption, indicating the existence of the hydrogen bond interactions between hydroxyl groups in phenol, BPA and 2-CP or oxygen-containing groups in DP and N-H groups in $\text{AgBr}@\text{Ag}/\text{N-RGO}$ [43]. The stretching vibration of $\text{C}=\text{C}$ band was shifted from 1615 to 1631 cm^{-1} after BPA sorption and to 1635 cm^{-1} after 2-CP sorption, suggesting the existence of the $\pi-\pi$ interaction between the two aromatics and N-RGO in $\text{AgBr}@\text{Ag}/\text{N-RGO}$ [43]. Moreover, the $\pi-\pi$ interaction was increased by the conjugating of the free-flowing π electrons from the sp^2 carbon of graphene with the long-pair electrons from the doped N atoms [25]. Therefore, the electron transfer process from pollutants to Ag could be accelerated by the Ag-N complex along the $\pi-\pi$ graphitic carbon network of N-RGO , resulting in the high photoactivity and photostability of $\text{AgBr}@\text{Ag}/\text{N-RGO}$.

4. Conclusions

The $\text{AgBr}@\text{Ag}/\text{N-RGO}$ photocatalyst with good interfacial contact was successfully prepared by a hydrothermal-*in situ* oxidation method. The visible-light-driven photoactivity of $\text{AgBr}@\text{Ag}/\text{N-RGO}$ was 20, 5.3, and 2.9 times higher than that of $\text{Ag}/\text{N-RGO}$, $\text{TiO}_{2-x}\text{N}_x$, and $\text{AgBr}@\text{Ag}$, respectively. The characterization results showed Ag NPs dispersedly anchored on N-RGO and enwrapped by AgBr . The good interfacial contact of AgBr , Ag and N-RGO promoted one electron transfer from Ag

Scheme 1. Proposed photocatalytic mechanism for $\text{AgBr}@\text{Ag}/\text{N-RGO}$.



to AgBr and further to N-RGO to generate O_2^- by reducing O_2 , and another electron transfer from organic pollutants to Ag by the Ag-N complex along the $\pi-\pi$ graphitic carbon network of N-RGO, leading to the fast and stable degradation and mineralization of various organic pollutants under visible light. These results suggest that AgBr@Ag/N-RGO is a promising visible-light-sensitive photocatalyst for removal of organic pollutants in wastewater.

Acknowledgments

This work was supported by National Key Research and Development Plan (2016YFA0203204) and the National Natural Science Foundation of China (Grant Nos. 51538013, 21407165).

Appendix A. Supplementary data

Supplementary data associated with this article can be found, in the online version, at <http://dx.doi.org/10.1016/j.apcatb.2017.08.038>.

References

- [1] L. Andronic, L. Isac, S. Miralles-Cuevas, M. Visa, I. Oller, A. Duta, S. Malato, Pilot-plant evaluation of TiO_2 and TiO_2 -based hybrid photocatalysts for solar treatment of polluted water, *J. Hazard. Mater.* 320 (2016) 469–478.
- [2] X. Yan, X. Zhu, R. Li, W. Chen, Au/BiOCl heterojunction within mesoporous silica shell as stable plasmonic photocatalyst for efficient organic pollutants decomposition under visible light, *J. Hazard. Mater.* 303 (2016) 1–9.
- [3] C.Y. Wang, X. Zhang, X.N. Song, W.K. Wang, H.Q. Yu, Novel $Bi_{12}O_{15}Cl_6$ photocatalyst for the degradation of bisphenol A under visible-light irradiation, *ACS Appl. Mater. Interfaces* 8 (2016) 5320–5326.
- [4] M. Wang, C. Gao, L. He, Q. Lu, J. Zhang, C. Tang, S. Zorba, Y. Yin, Magnetic tuning of plasmonic excitation of gold nanorods, *J. Am. Chem. Soc.* 135 (2013) 15302–15305.
- [5] Z. Zheng, T. Tachikawa, T. Majima, Single-particle study of Pt-modified Au nanorods for plasmon-enhanced hydrogen generation in visible to near-infrared region, *J. Am. Chem. Soc.* 136 (2014) 6870–6873.
- [6] Z. Bian, T. Tachikawa, P. Zhang, M. Fujitsuka, T. Majima, Au/ TiO_2 superstructure-based plasmonic photocatalysts exhibiting efficient charge separation and unprecedented activity, *J. Am. Chem. Soc.* 136 (2014) 458–465.
- [7] L. Liu, S. Ouyang, J. Ye, Gold-nanorod-photosensitized titanium dioxide with wide-range visible-light harvesting based on localized surface plasmon resonance, *Angew. Chem. Int. Ed.* 52 (2013) 6689–6693.
- [8] H. Yu, G. Cao, F. Chen, X. Wang, J. Yu, M. Lei, Enhanced photocatalytic performance of Ag_3PO_4 by simultaneous loading of Ag nanoparticles and Fe(III) cocatalyst, *Appl. Catal. B: Environ.* 160–161 (2014) 658–665.
- [9] Y. Tang, Z. Jiang, G. Xing, A. Li, P.D. Kanhere, Y. Zhang, T.C. Sum, S. Li, X. Chen, Z. Dong, Efficient Ag@AgCl cubic cage photocatalysts profit from ultrafast plasmon-induced electron transfer processes, *Adv. Funct. Mater.* 23 (2013) 2932–2940.
- [10] W. Wang, L. Jing, Y. Qu, Y. Luan, H. Fu, Y. Xiao, Facile fabrication of efficient AgBr- TiO_2 nanostructured photocatalyst for degrading pollutants and its photo-generated charge transfer mechanism, *J. Hazard. Mater.* 243 (2012) 169–178.
- [11] J. Song, I. Lee, J. Roh, J. Jang, Fabrication of Ag-coated AgBr nanoparticles and their plasmonic photocatalytic applications, *RSC Adv.* 4 (2014) 4558–4563.
- [12] S. Song, B. Cheng, N. Wu, A. Meng, S. Cao, J. Yu, Structure effect of graphene on the photocatalytic performance of plasmonic Ag/ Ag_2CO_3 -RGO for photocatalytic elimination of pollutants, *Appl. Catal. B: Environ.* 181 (2016) 71–78.
- [13] H. Sun, Y. Wang, S. Liu, L. Ge, L. Wang, Z. Zhu, S. Wang, Facile synthesis of nitrogen doped reduced graphene oxide as a superior metal-free catalyst for oxidation, *Chem. Commun.* 49 (2013) 9914–9916.
- [14] X. Xie, J. Long, J. Xu, L. Chen, Y. Wang, Z. Zhang, X. Wang, Nitrogen-doped graphene stabilized gold nanoparticles for aerobic selective oxidation of benzylic alcohols, *RSC Adv.* 2 (2012) 12438–12446.
- [15] Y. Liang, Y. Li, H. Wang, J. Zhou, J. Wang, T. Regier, H. Dai, Co_3O_4 nanocrystals on graphene as a synergistic catalyst for oxygen reduction reaction, *Nat. Mater.* 10 (2011) 780–786.
- [16] Y. Xu, H. Bai, G. Lu, C. Li, G. Shi, Flexible graphene films via the filtration of water-soluble noncovalent functionalized graphene sheets, *J. Am. Chem. Soc.* 130 (2008) 5856–5857.
- [17] G. Barolo, S. Livraghi, M. Chiesa, M.C. Paganini, E. Giamello, Mechanism of the photoactivity under visible light of N-doped titanium dioxide. Charge carriers migration in irradiated N- TiO_2 investigated by electron paramagnetic resonance, *J. Phys. Chem. C* 116 (2012) 20887–20894.
- [18] O.C. Compton, S.T. Nguyen, Graphene oxide, highly reduced graphene oxide, and graphene: versatile building blocks for carbon-based materials, *Small* 6 (2010) 711–723.
- [19] Y. Zhou, S. Ren, Q. Dong, Y. Li, H. Ding, One-pot preparation of Bi/Bi₂WO₆/reduced graphene oxide as a plasmonic photocatalyst with improved activity under visible light, *RSC Adv.* 6 (2016) 102875–102885.
- [20] Q. Li, B. Guo, J. Yu, J. Ran, B. Zhang, H. Yan, J.R. Gong, Highly efficient visible-light-driven photocatalytic hydrogen production of CdS-cluster-decorated graphene nanosheets, *J. Am. Chem. Soc.* 133 (2011) 10878–10884.
- [21] Md.S. Shah, W. Kim, J. Park, D.K. Rhee, I. Jang, N. Park, J.Y. Lee, P.J. Yoo, Highly efficient and recyclable nanocomplexed photocatalysts of AgBr/N-doped and amine-functionalized reduced graphene oxide, *ACS Appl. Mater. Interfaces* 6 (2014) 20819–20827.
- [22] Y.S. Xu, W.D. Zhang, Ag/AgBr-grafted graphite-like carbon nitride with enhanced plasmonic photocatalytic activity under visible light, *ChemCatChem* 5 (2013) 2343–2351.
- [23] S. Sandoval, N. Kumar, J. Oro-Solé, A. Sundaresan, C.N.R. Rao, A. Fuertes, G. Tobias, Tuning the nature of nitrogen atoms in N-containing reduced graphene oxide, *Carbon* 96 (2016) 594–602.
- [24] L.C. Sim, K.H. Leong, S. Ibrahim, P. Saravanan, Graphene oxide and Ag engulfed TiO_2 nanotube arrays for enhanced electron mobility and visible-light-driven photocatalytic performance, *J. Mater. Chem. A* 2 (2014) 5315–5322.
- [25] D. Du, P. Li, J. Ouyang, Nitrogen-doped reduced graphene oxide prepared by simultaneous thermal reduction and nitrogen doping of graphene oxide in air and its application as an electrocatalyst, *ACS Appl. Mater. Interfaces* 7 (2015) 26952–26958.
- [26] X. Wang, Y. Qin, L. Zhu, H. Tang, Nitrogen-doped reduced graphene oxide as a bifunctional material for removing bisphenols: synergistic effect between adsorption and catalysis, *Environ. Sci. Technol.* 49 (2015) 6855–6864.
- [27] H. Zhang, X. Fan, X. Quan, S. Chen, H. Yu, Graphene sheets grafted Ag@AgCl hybrid with enhanced plasmonic photocatalytic activity under visible light, *Environ. Sci. Technol.* 45 (2011) 5731–5736.
- [28] H. Yu, W. Chen, X. Wang, Y. Xu, J. Yu, Enhanced photocatalytic activity and photoinduced stability of Ag-based photocatalysts: the synergistic action of amorphous-Ti(IV) and Fe(III) cocatalysts, *Appl. Catal. B: Environ.* 187 (2016) 163–170.
- [29] S.G. Aspromonte, M.D. Mizrahi, F.A. Schneeberger, J.M.R. López, A.V. Boix, Study of the nature and location of silver in Ag-exchanged mordenite catalysts. Characterization by spectroscopic techniques, *J. Phys. Chem. C* 117 (2013) 25433–25442.
- [30] P. Christopher, H. Xin, S. Linic, Visible-light-enhanced catalytic oxidation reactions on plasmonic silver nanostructures, *Nat. Chem.* 3 (2011) 467–472.
- [31] H.Y. Hu, Z.B. Jiao, G.X. Lu, J.H. Ye, Y.P. Bi, Enhanced photocatalytic properties of biomimetic Ag/AgCl heterostructures, *RSC Adv.* 4 (2014) 31795–31798.
- [32] G. Dai, J. Yu, G. Liu, A new approach for photocorrosion inhibition of Ag_2CO_3 photocatalyst with highly visible-light-responsive reactivity, *J. Phys. Chem. C* 116 (2012) 15519–15524.
- [33] C. Hu, T. Peng, X. Hu, Y. Nie, X. Zhou, J. Qu, H. He, Plasmon-induced photo-degradation of toxic pollutants with Ag-AgI/ Al_2O_3 under visible-light irradiation, *J. Am. Chem. Soc.* 132 (2010) 857–862.
- [34] Y. Dai, Y. Sun, J. Yao, D. Ling, Y. Wang, H. Long, X. Wang, B. Lin, T.H. Zeng, Y. Sun, Graphene-wrapped TiO_2 nanofibers with effective interfacial coupling as ultrafast electron transfer bridges in novel photoanodes, *J. Mater. Chem. A* 2 (2014) 1060–1067.
- [35] K. Sivula, R. Zboril, F. Le Formal, R. Robert, A. Weidenkaff, J. Tucek, J. Frydrych, M. Gratzel, Photoelectrochemical water splitting with mesoporous hematite prepared by a solution-based colloidal approach, *J. Am. Chem. Soc.* 132 (2010) 7436–7444.
- [36] F. Meng, J. Li, S.K. Cushing, M. Zhi, N. Wu, Solar hydrogen generation by nanoscale p-n junction of p-type molybdenum disulfide/n-type nitrogen-doped reduced graphene oxide, *J. Am. Chem. Soc.* 135 (2013) 10286–10289.
- [37] Y.Y. Bai, F.R. Wang, J.K. Liu, A new complementary catalyst and catalytic mechanism: Ag_2MoO_4 /Ag/AgBr/GO heterostructure, *Ind. Eng. Chem. Res.* 55 (2016) 9873–9879.
- [38] H. Cheng, B. Huang, Y. Dai, X. Qin, X. Zhang, One-step synthesis of the nanostuctured AgI/BiOI composites with highly enhanced visible-light photocatalytic performances, *Langmuir* 26 (2010) 6618–6624.
- [39] J. Cao, B. Xu, B. Luo, H. Lin, S. Chen, Preparation, characterization and visible-light photocatalytic activity of AgI/AgCl/ TiO_2 , *Appl. Surf. Sci.* 257 (2011) 7083–7089.
- [40] Y. Fan, W. Ma, D. Han, S. Gan, X. Dong, L. Niu, Convenient recycling of 3D AgX /graphene aerogels ($X = Br, Cl$) for effi cient photocatalytic degradation of water pollutants, *Adv. Mater.* 27 (2015) 3767–3773.
- [41] Y. Hou, X. Li, Q. Zhao, G. Chen, C. Raston, Role of hydroxyl radicals and mechanism of escherichia coli inactivation on Ag/AgBr/ TiO_2 nanotube array electrode under visible light irradiation, *Environ. Sci. Technol.* 46 (2012) 4042–4050.
- [42] P. Wang, Y. Tang, Z. Dong, Z. Chen, T.T. Lim, Ag-AgBr/ TiO_2 /RGO nanocomposite for visible-light photocatalytic degradation of penicillin G, *J. Mater. Chem. A* 1 (2013) 4718–4727.
- [43] S. Yu, X. Wang, W. Yao, J. Wang, Y. Ji, Y. Ai, A. Alsaedi, T. Hayat, X. Wang, Macroscopic spectroscopic, and theoretical investigation for the interaction of phenol and naphthol on reduced graphene oxide, *Environ. Sci. Technol.* 51 (2017) 3278–3286.